



## OPEN Design and analysis of innovative multi-frequency ultrasonic probe characteristics

Yu-Lin Song<sup>1,2✉</sup>, Tzu-Zin Lin<sup>2</sup>, Shih Hsun Tu<sup>3</sup> & Alexander Stiegler<sup>3</sup>

This study presents the development of a novel multifrequency ultrasound probe distinguished by its broad bandwidth and high sensitivity. A comprehensive investigation was conducted using theoretical analysis, numerical simulations, and experimental validation to characterize the probe's multiband performance through the effective electromechanical coupling coefficient (ECct). The probe satisfies the bandwidth requirements for skin tissue detection, demonstrating potential for applications such as automated injections. Finite element simulations were employed to determine the resonance conditions of the layered piezoelectric structure, informing the probe's design and fabrication process. Impedance analysis identified resonant frequencies at 1.70, 2.44, 3.10, 4.53 and 7.16 MHz. The probe exhibited a linear acoustic response exceeding 5 MPa and achieved an electromechanical coupling coefficient below 0.5, underscoring its superior penetration capability and overall performance.

**Keywords** Ultrasonic device, Impedance analysis, Adjustable frequency, Piezoelectric

Ultrasound probes and handheld acoustic imaging devices are widely used for in vivo organ imaging. However, their applications extend beyond this domain, such as in developing an autonomous subcutaneous drug injection syringe to ensure safer patient self-injection. An essential feature of such an auto-injector would be its ability to identify a safe path through the skin for the hypodermic needle, a task that can be effectively performed using an ultrasound probe. In vivo imaging probes typically operate in B-mode within the frequency range of 1–16 MHz<sup>1</sup>. However, multifrequency ultrasound probes may employ A-mode to achieve more precise positioning and depth information, which is advantageous for applications like the proposed auto-injector.

According to Bezugly et al.,<sup>2</sup> 22 MHz HFUS waves can penetrate to a depth of 9 mm, 33 MHz up to 7 mm, and 75 MHz up to 3.5 mm. The frequency range of probe oscillation typically lies between 10 MHz and 100 MHz, depending on the application needs. High-frequency ultrasound (HFUS) probes oscillate at these frequencies to provide higher resolution, although this requires sophisticated manufacturing processes<sup>2</sup>. One common oscillatory mode is half-wavelength oscillation. In this study, we use half-wavelength frequency, with a needle length of 4 mm for subcutaneous injection, inferring that the upper frequency limit tested is 10 MHz, the limit of the applicable test fixture (Keysight E4990A). Wang et al. demonstrated the classification of grayscale ultrasound nodules validated through pathological examinations and the electromechanical coupling coefficient (ECct) obtained from echo morphology. The main parameters influencing ultrasound results are frequency, peak intensity, and signal duration<sup>3</sup>. Various parameter combinations may be necessary for ultrasound-based detection of the epidermis and dermis.

This study aims to develop a multiband transceiver as an ultrasound probe for auto-injector applications. Such a probe must be compact and capable of multifrequency operations. We choose the resonant frequency to ensure high power output as demonstrated by Liu et al.<sup>4</sup> who employed piezoelectric ceramics to induce modal oscillation along the thickness direction, reducing driving frequency and minimizing losses. Model analysis and parameter optimization were performed using the multiphysics finite element simulation software COMSOL (version 6.2), as described by Shu<sup>5</sup>. The motivation behind this study is to enhance the precision of automatic injection systems, enabling accurate measurement of various subcutaneous depths. Traditional single-frequency probes often fall short in providing the detailed information needed for diverse applications. In contrast, multi-frequency probes can accurately measure different depths and tissue types, crucial for improving the accuracy and safety of injections. This research leverages multi-frequency ultrasonic probes to ensure precise detection and reliable performance, particularly for non-pierceable tissues such as lymphatic vessels, blood vessels, and bones.

<sup>1</sup>Department of Computer Science and Information Engineering, Asia University, Taichung 413, Taiwan.

<sup>2</sup>Department of Bioinformatics and Medical Engineering, Asia University, Taichung 413, Taiwan. <sup>3</sup>SHL Medical, Taoyuan 338, Taiwan. ✉email: d87222007@ntu.edu.tw

Solid silver thickness	20 μm
Solid silver content	More than 50% after drying
Viscosity	10,000–25,000 CPS (depending on room temperature)
Impedance	0.07 Ω/ in^2 (standard test resistance 50Ω)
Shelf life	6 months when sealed at 22°C, longer at 5°C
Methanol can be used as a diluent	

**Table 1.** Silver glue ingredients.



**Fig. 1.** Mesh side cutting diagram of piezoelectric material.

Our design incorporates crucial elements, such as the dimensions of piezoelectric materials, modal analysis, multi-physics coupling, and impedance analysis, all impacting ultrasonic frequencies. We designed five types of probes operating within the range of 1 to 10 MHz to meet diverse measurement requirements. Performance simulations and analyses using COMSOL Multiphysics guarantee the stability, seamless integration, and ease of fabrication of the probes. This study makes significant contributions, including improving clinical applications of medical signals, achieving stable measurements with the ultrasound probe to generate A-mode signals, and enhancing the precision of automated injection systems while reducing medical risks. Notably, we introduce multi-band probes with varying layer thicknesses to create a composite ultrasonic probe. By comparing simulated and experimental impedance diagrams through modal analysis, we identify patterns and extract crucial data. These results facilitate the safe use of the technology by non-medical personnel, improving injection efficiency and ensuring safety and stability in clinical applications.

**Design and simulation of the novel ultrasonic transducer**

The thickness of a piezoelectric material is linked to its resonance frequency. The piezoelectric materials in this study were designed through COMSOL simulations.

**Ultrasonic transducer design**

A series of three-dimensional (3D) models were developed to represent the ultrasound probe for the analysis of the resonance behavior of various piezoelectric materials. The geometric dimensions were designed in accordance with standard radial designs<sup>6</sup>. Each model had strong coupling material characteristics under specific resonance modes. Geometric shapes with smaller ECCt values were prioritized. (See Eq. 2.1) The free resonance state of a 3D object is complex and difficult to analyze; therefore, the simulation environment was simplified by setting the overall damping, assuming that displacement, velocity, and density values were continuous within the ultrasonic transducer material, and setting the boundary condition of the piezoelectric element as its natural oscillation state. Consequently, the oscillation of the piezoelectric element’s central axis was directional, and vibrations in the normal and cross-sectional directions were independent.

$$ECCt = \sqrt{\frac{Stored\ Mechanical\ Energy}{Total\ Stored\ Energy}} \tag{1}$$

*Piezoelectric element and perfectly matched layer mesh*

To avoid distortion, the simulation assumed that charge remained on the surface of the PZT. The PZT ceramic was coated with a layer of silver glue (please see Table 1 for parameters) to enhance its conductivity, with the thickness of the silver glue being approximately 5% of that of the piezoelectric element. This setting helps maintain simulation fidelity. The layers were considered to be sliced in different directions according to the simulation dimensions<sup>7</sup>. Fig. 1 presents both the odd and even slicing configurations. The cross-sectional cutting method is as shown in Fig. 1.

Based on wavelength calculations, the thickness of the silver glue is closely related to the operating frequency of the PZT ceramic. In general experimental designs, the thickness of the conductive layer is set as a portion of the wavelength. Once the operating frequency is known, the wavelength in the medium can be calculated using the formula based on the speed of sound in the medium. According to the research, the thickness  $d$  of the silver glue layer can be set as a portion of the wavelength, expressed as:

$$d = k \cdot \lambda \tag{2}$$

Where  $k$  typically ranges from 0.1 to 0.25, with the assumption here being  $k = 0.1 \lambda$ . On the other hand, the impedance  $Z$  of the layered structure can be expressed in terms of thickness and material characteristics. The thickness of the PZT ceramic stack combined with the silver glue conductive layer affects the overall impedance. The effective impedance  $Z_{eff}$  can be modeled as:

$$Z_{eff} = \frac{Z_{PZT} \cdot Z_{Ag}}{Z_{PZT} + Z_{Ag}} \tag{3}$$

where  $Z_{PZT}$  is the impedance of the piezoelectric material, and  $Z_{Ag}$  is the impedance of the silver layer. The above expressions for wavelength-based thickness calculations and impedance-related considerations ensure that the thickness of the silver glue is optimized, thereby enhancing performance while maintaining simulation fidelity.

In finite element method (FEM) calculations, the domain must be defined by setting boundary conditions, such as a constant potential. For the FEM model in this study, the domain boundaries were assumed to have low reflectivity; that is, they were assumed to absorb outgoing propagating waves without generating spurious reflections. Sound field reflectivity is the ratio of the reflected sound energy to the incident sound energy when a sound wave encounters an obstacle or medium interface, describing the efficiency of sound wave reflection. Moreover, the boundaries were assumed to have a finite impedance with respect to a reference at infinity. Please refer to Table 2 for model impedance parameters. The perfectly matched layer (PML) mesh was therefore selected, which acts as an ideal absorber. Detailed low reflectivity settings will be mentioned in Chap. (3.2.3).

Circuit design

A circuit was simulated to receive signals from the probe, which were modeled as Gaussian-modulated sinusoidal waves with their center frequency set to the natural frequency of the sample. The circuit simulation involved adding terminal nodes in the electrostatic interface, setting the terminal type to “circuit,” establishing boundaries for electrodes and electrical connections, forming loop connections between electrodes and electrical connection boundaries, adding a ground node on the electrostatic interface and applying it to another electrode, and finally adding an external terminal node in the circuit interface and setting it as an “Electrical” endpoint. The voltage between the terminal nodes represented the circuit potential.

Piezoelectric ceramic materials

The two surfaces of a piezoelectric element serve as independent oscillators, resonating at a thickness  $L = n \frac{\lambda_p}{2}$ , where  $\lambda_p$  represents the wavelength related to the speed of sound in the transducer material and is an odd integer representing different resonance modes<sup>9</sup>. This resonance should be less than 42 MHz to achieve the high frequency necessary for subcutaneous imaging. Therefore, to match the natural oscillation of half wavelength, the thickness of the first PZT layer was set to 0.28 mm. The structural mechanics and acoustic modules in COMSOL were used to configure the characteristics of the piezoelectric material.

Resonance simulation settings

The devices’ operational frequencies were selected as 7.05, 4.9, 3.3, 2.4, and 1.9 MHz. The Solid Mechanics and Electrostatics modules of COMSOL were used to model piezoelectric materials (please see Table 3) and charge conservation. The piezoelectric module enables setting electric potential boundary conditions on the surface of the piezoelectric material. COMSOL was also used for electro mechanical coupling computations.

Tissue	Density (g/cm <sup>3</sup> )	Speed of sound (m/s)	Acoustic impedance [(kg/m <sup>2</sup> ·s)] ×106
Water	1.00	1480	1.48
Bone	1.90	4000	7.6
Blood	1.05	1575	1.66
Fat	0.95	1450	1.38
Liver	1.06	1590	1.69
Muscle	1.06	1575	1.68
Skin	1.15	1730	1.99
Air	0.001184	334	0.43

Table 2. Density and velocity of sound in the medium, characteristic impedance<sup>8</sup>.

Type	Value						Unit
Elasticity matrix, voigt symbol	$1.12 \times 10^{11}$	$8.02 \times 10^{10}$	$8.47 \times 10^{10}$	0	0	0	Pa
	$802 \times 10^{10}$	$1.27 \times 10^{11}$	$8.47 \times 10^{10}$	0	0	0	
	$8.47 \times 10^{10}$	$8.47 \times 10^{10}$	$1.17 \times 10^{11}$	0	0	0	
	0	0	0	$2.30 \times 10^{10}$	0	0	
	0	0	0	0	$2.30 \times 10^{10}$	0	
	0	0	0	0	0	$2.35 \times 10^{10}$	
Coupling matrix, voigt symbol	0	0	0	0	17.0345	0	C/m <sup>2</sup>
	0	0	0	17.0345	0	0	
	-6.62281	-6.62281	23.2403	0	0	0	
Relative permittivity	3130		0		0		1
	0		3130		0		
	0		0		2100		

Table 3. Strain parameters of PZT5H piezoelectric material.

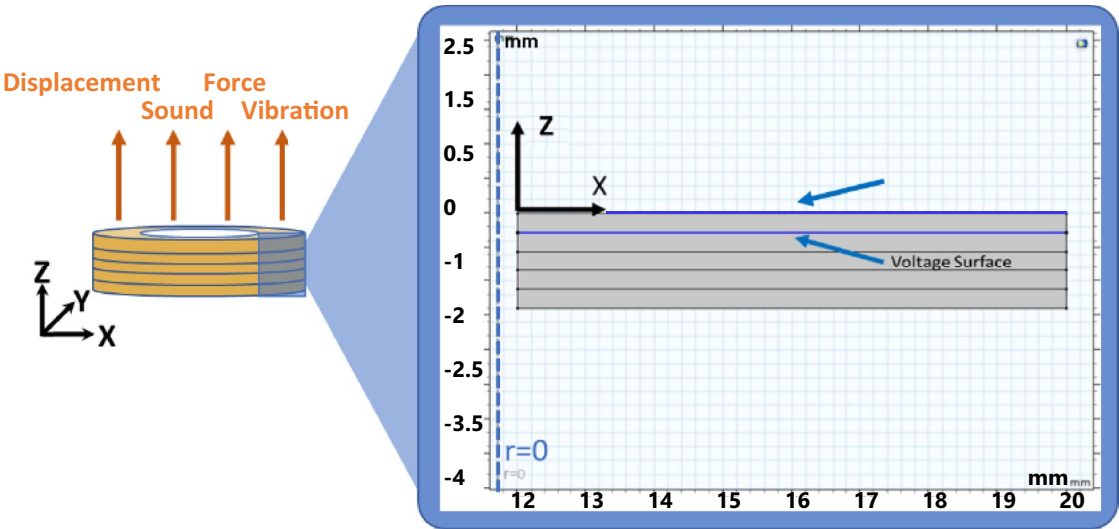


Fig. 2. Schematic diagram of 2D simulation.  $r=0$  mm, which is axisymmetric.

Tissue	Density (kg/m <sup>3</sup> )	Velocity (m/s)	Nonlinearization parameters
Bone	1908	4000	7.4

Table 4. Phantom material parameters.

Geometry setup and parameter selection

A two-dimensional (2D) simulation was first conducted to reduce computational complexity, after which it was expanded to a 3D model. The resonance direction was set along the y-axis, as displayed in Fig. 2. For a resonance frequency of 7.5 MHz, the simulated piezoelectric material’s single-layer thickness was 0.28 mm, and its density was 7500 kg/m<sup>3</sup>. Please see Table 4. The material was polarized along the y-axis.

Simulate the experimental setting

A central symmetric axis was defined, and the boundary condition was set as a free-surface boundary. The voltage source for the circuit was a Gaussian-modulated sine wave. The piezoelectric element’s impedance frequency response was simulated using a 3D model as 3D simulations offer greater fidelity than do 2D simulations. The following subsection discusses piezoelectric effects, acoustic equations, and perfectly matched layer (PML) technique. Additionally, the parameters and boundary conditions for the COMSOL simulations are elaborated upon.

### Piezoelectric material equations in COMSOL

The constitutive equations in COMSOL include those for piezoelectric effects as well as the mechanical and electrical anisotropy of a material. After specifying the matrices for these equations, COMSOL identifies which equation domains should be used within each FEM unit.

The piezoelectric equations describe the coupled relationship between stress or strain and electric field polarization in a piezoelectric material:

$$\begin{cases} S_p = s_{pq}^E \sigma_q + d_{pi}^E E_i \\ D_i = d_{ip} \sigma_p + \epsilon_{ij}^E E_j \end{cases} \quad (4)$$

In the preceding equation, the subscripts  $i, j=1,2,3$  and  $p, q=1, 2, \dots, 6$  represent different directions in the material's coordinate system.  $S_p$ ,  $\sigma_q$ , and  $\sigma_p$  denote the strain, stress, and transpose stress vectors of the piezoelectric elastic body, respectively, and  $s_{pq}^E$  denotes the compliance coefficient matrix.  $D_p$ ,  $E_p$ , and  $E_j$  represent the electric displacement, electric field intensity, and transposed electric field intensity vectors of the piezoelectric body, respectively, and  $\epsilon_{ij}^E$ ,  $d_{pp}$ , and  $d_{ip}$  represent the piezoelectric and dielectric constant matrices. If the Poisson effect is neglected and only the piezoelectric polarization in the thickness direction (direction 3) is considered, the equation can be simplified as Eq. (5):

$$\begin{cases} S_3 = s_{33}^E \sigma_3 + d_{33}^E E_3 \\ D_3 = d_{33} \sigma_3 + \epsilon_{33}^E E_3 \end{cases} \quad (5)$$

For a piezoelectric stack comprising multiple piezoelectric layers and neglecting energy losses between the layers, the total output displacement can be modeled as the linear superposition of the displacements of each ceramic layer. Therefore, the expression  $S_3 = s_{33}^E \sigma_3 + d_{33}^E E_3$  in the preceding equation can be rewritten as Eq. (6):

$$\frac{\delta}{nt} = s_{33}^E \frac{(-T)}{A} + d_{33} \frac{U}{t} \quad (6)$$

where  $\delta$  represents the total output displacement of the piezoelectric stack,  $t$  is the thickness of a single layer,  $T_3$  is the pressure in the thickness direction,  $A$  is the cross-sectional area of the stack, and  $U$  is the applied voltage,  $T_3$  refers to the component of mechanical stress in the third direction.

Equation (6) can be translated into a deformation expression as Eq. (7):

$$\delta = nd_{33}U - \frac{T_3}{k_3} \quad (7)$$

where  $k_3 = A/(s_{33}^E nt)$ . This equation describes the equivalent static stiffness in the thickness direction of the piezoelectric stack, which is determined by the intrinsic properties of the piezoelectric material. In this study, the values were obtained through simulations. If  $T_3 = 0$ , the deformation of the piezoelectric stack is maximized; this is referred to as free displacement ( $\delta_{\text{free}} = nd_{33}U$ ). Conversely, if the deformation  $\delta = 0$ , the equivalent load is maximized; this is known as the blocking force ( $T_{\text{max}} = k_3 nd_{33}U$ ).

### Acoustic equations in COMSOL

The acoustic equations were set in COMSOL for A-mode imaging, which uses multicycle pulses. Echoes returning from the tissue are detected by the multifrequency probe, amplified, and processed for display. The pressure waves emitted by the piezoelectric sensor (transducer) in the body cavity follow the solution of the wave equation in the time domain:

$\nabla^2 p(r, t) - \frac{1}{c^2} \frac{\partial^2 p(r, t)}{\partial t^2} = 0$ , where  $p(r, t)$  represents pressure and  $c$  represents the speed of sound in the medium.

To avoid interference resulting in range ambiguity, signals from the target of interest must be received before the next pulse is transmitted. Thus, the transceiver must be coupled with a water-like medium, and their acoustic impedances should match. The propagation of the acoustic field in the piezoelectric material must also be considered.

The wave equation can be solved to obtain the natural frequency of the piezoelectric material as Eq. (8):

$$\nabla \cdot \left( -\frac{1}{\rho_c} \nabla p \right) + \frac{\lambda^2 \rho}{\rho_c c^2} = 0 \quad (8)$$

In this equation,  $\lambda$  denotes eigenvalues that are related to the characteristic frequency and angular frequency by  $\lambda = \frac{\omega}{2\pi f} = \frac{1}{\omega}$ . These eigenvalues are independent of pressure; therefore, a solver can compute the solution for this coupled eigenvalue problem. Periodic oscillations can be represented by sinusoidal waves.

### *Perfectly matched layer (PML) technique<sup>10</sup>*

PML (Perfectly Matched Layer) technology is used to absorb wave propagation in numerical simulations to prevent waves from being reflected at the boundaries of the calculation domain, thus affecting the calculation results. In wave problems, the sound pressure  $P_a$  is decomposed into its components in different directions: x component, y component, and z component. When explaining PML technology, attention is given to the propagation of waves in different directions and their damping in the PML region, as well as the components of sound pressure and the direction of propagation. The x component of sound pressure  $P_{ax}$  can be seen as a plane wave propagating only in the x direction. In the PML region,  $P_{ax}$  is damped by the damping coefficient  $\sigma_x$ . The PML area dampens the sound pressure component, gradually absorbing the waves upon entering the PML area to avoid reflection at the interface. This is achieved by selecting appropriate damping coefficients  $\sigma_x$ ,  $\sigma_y$ , and  $\sigma_z$ . Impedance matching and non-reflection interface settings are done through impedance matching to ensure that the wave does not reflect back at the interface when propagating to the PML area, creating a reflection-free interface and achieving the goals of PML. In the 1D case, only the damping in one direction needs consideration; in the 2D and 3D cases, the damping in each direction needs separate consideration. Lastly, there is the Helmholtz equation and complex coordinate transformation. A key method of PML technology is to map the solution of the Helmholtz equation from real coordinate space to complex coordinate space, enabling an analytical continuation solution. By introducing complex variable changes, wave energy can be efficiently absorbed within the PML region. In essence, the core of PML technology is to absorb wave energy through damping coefficients and prevent reflections at the boundaries of the computational domain, thereby enhancing the accuracy of numerical simulations. In finite element method (FEM) calculations, the domain must be defined by setting boundary conditions, such as a constant potential. This ensures the absorption of outgoing propagating waves without generating spurious reflections. Additionally, the boundaries were assumed to have a finite impedance concerning a reference at infinity. Therefore, the perfectly matched layer (PML) mesh was selected, serving as an ideal absorber.

**Time-domain PML thickness criteria** In time-domain simulations, the physical thickness of the PML plays a critical role in the effective absorption of outgoing waves. Unlike frequency-domain models, time-domain PMLs do not employ real coordinate stretching, making their geometric size directly influential. Therefore, it is recommended to set the PML thickness to accommodate at least 6 layers for polynomial scaling and 8 layers for rational scaling, using mesh elements of similar size to those in the adjacent physical domain. These mesh settings help reduce spurious reflections by ensuring smooth wave attenuation. Moreover, the scaling factor and curvature parameter settings (commonly 1,3 for polynomial and 1,1 for rational) are essential to maintain a theoretical reflection coefficient  $R_0 = 10^{-3}$  at the interface. Failure to provide sufficient thickness or correct scaling may result in partial reflection and degrade simulation accuracy.

**Avoiding non-physical reflection via stretching optimization** In frequency-domain simulations, the PML utilizes real coordinate stretching to absorb outgoing propagating and evanescent waves. However, when the PML is placed too close to a radiating source or scattering boundary, evanescent waves may interact with the stretching region, producing non-physical reflections. This phenomenon is particularly significant when the mesh geometry is highly irregular or when the coordinate stretching parameters are not optimized.

To avoid such effects, it is generally advised to place the PML at least  $\lambda/8$  away from sources or scatterers, though this is not strictly necessary if the stretching factor, scaling, and curvature are carefully tuned. These adjustments ensure that the PML effectively suppresses both traveling and near-field wave components without introducing reflection artifacts. Additionally, structured meshing within the PML region enhances stability and performance.

## **Ultrasonic probe simulation and experiment discussion**

### **PZT simulated oscillations**

After excitation, the piezoelectric element vibrates along the Z-axis (the third direction in Cartesian coordinates), where the maximum displacement occurs at the center in this thickness direction. When the probe vibrates upward (i.e., in the z direction), the vibration direction is consistent (Fig. 3). The frequency of this upward vibration is the material's natural frequency and falls within the working frequency range associated with the  $d_{33}$  material properties of PZT. At the optimal position, the displacement during vibration is maximized, improving the transmission of sound waves through the ceramic.

Sensors are typically developed by first selecting a shape and then deducing its vibration pattern<sup>11</sup>; by contrast, multifrequency ultrasound probes are designed by first selecting a desired vibration pattern and then developing a shape. The stress concentration inside the multilayered piezoelectric material stack affects its reliability<sup>12</sup>. In particular, high-frequency large tensile stress can lead to damage<sup>13</sup>. Therefore, analyzing and optimizing the stress distribution inside the stack is essential to identify areas of maximum stress and ensure that the designed multilayer probe is reliable<sup>14</sup>.

In order to visualize the mechanical response of the piezoelectric stack under electrical excitation, Fig. 3 illustrates a complete vibration cycle of the PZT layer in four stages: (a) excitation, (b) steady-state oscillation, (c) relaxation, and (d) re-excitation. The stress and strain distributions within the multilayer stack are shown using solid lines (Initial state) and dashed lines (Vibration) to distinguish the dynamic deformation from the original geometry.

This cycle emphasizes how the internal layers of the piezoelectric stack undergo periodic tensile and compressive stresses, particularly along the Z-axis (thickness direction). These internal stress variations, if not well-distributed, may lead to stress concentration zones that affect the mechanical reliability of the device.



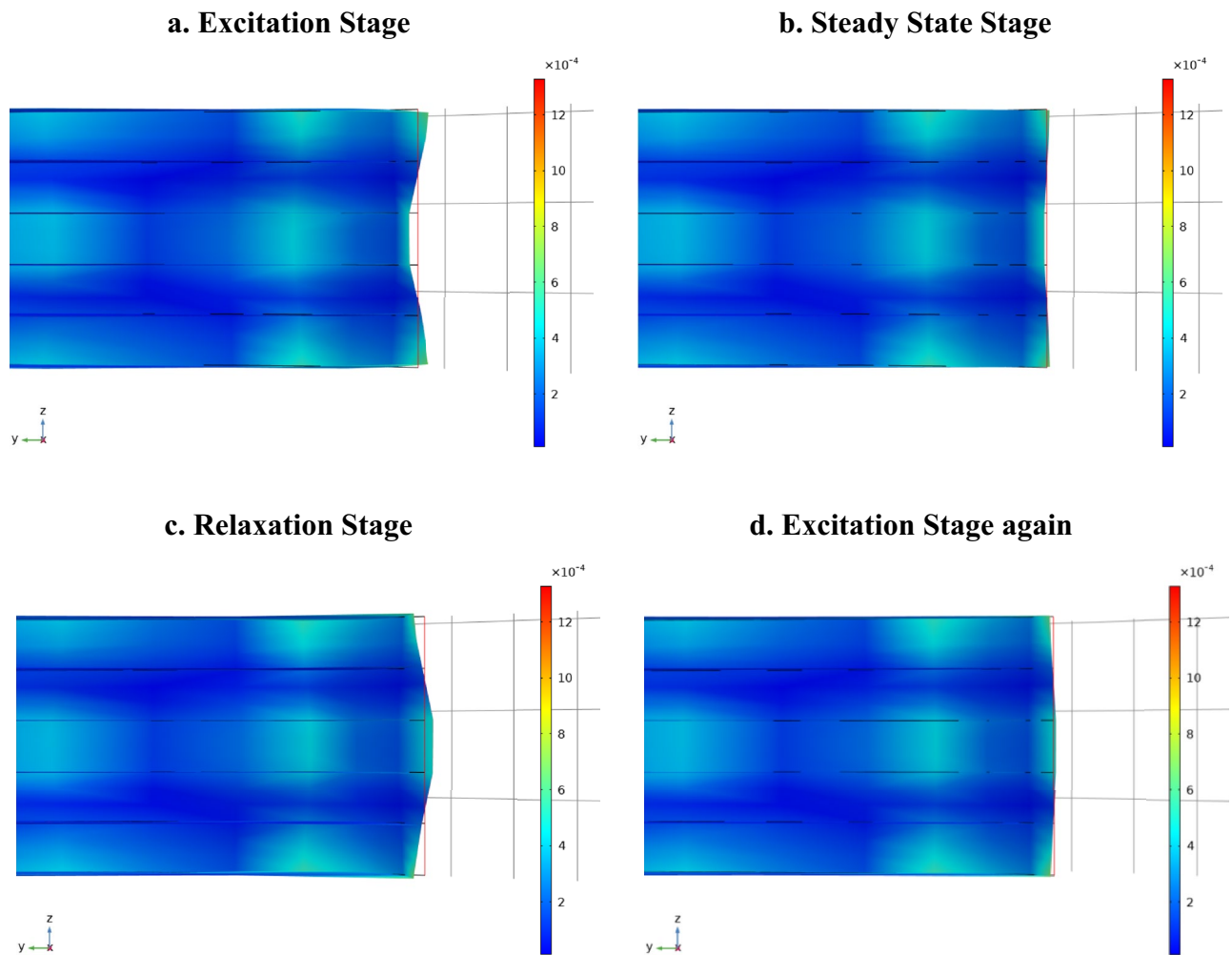


**Fig. 3.** Sequential illustration of a full vibration cycle of the PZT element under periodic excitation. Subfigures (a)–(d) correspond to successive phases in a cyclic oscillation process, revealing internal stress variations in the multilayer stack. The operating frequency of this picture is 1.90 MHz.

Therefore, capturing this dynamic evolution through COMSOL simulation is essential for understanding structural stability and ensuring the safe operation of the multilayer ultrasonic probe.

### Frequency domain impedance simulation

In this study, frequency domain simulations are utilized to analyze the samples. Each piezoelectric layer has a thickness of 0.28 mm. Figure 4 illustrates the impedance and phase angle of the ultrasonic probe over time, showing resonance frequencies and anti-resonance frequencies. The oscillation frequencies for each layer are 1.90, 2.40, 3.30, 4.90 and 7.05 MHz, respectively.

Each layer will only open one-color electrical path at a time, and in a multi-frequency environment, the frequency will switch. Each switch produces a different wavelength frequency, as shown in Fig. 4f, ranging from red in the first layer to violet in the fifth layer. The frequency switching is achieved through circuit electrification. Increasing the number of piezoelectric layers decreases the frequency and resolution but increases the intensity and penetration depth. As shown in Fig. 4, as the target operating frequency decreases, this study considered significant impedance states at different operating frequencies. The horizontal lines of the phase angle gradually become clearer, indicating that the oscillation modes involved in the piezoelectric effect become complete and more continuous, thereby enhancing the reference value of the phase angle. This correlation stems from the robust electromechanical coupling inherent in piezoelectric materials. Although the phase angle is categorized as an electrical parameter, it is directly influenced by the underlying mechanical vibrational dynamics. At or near resonance, the energy transfer between electrical input and mechanical motion is maximally efficient, resulting in substantial alterations in impedance phase behavior. This phenomenon facilitates the observation of mechanical mode formation through electrical measurements. Figure 4f illustrates the schematic of this device, including the multiple signal line circuits connected to the multi-layer oscillator. It is important to emphasize that switching plays a crucial role in this process because it allows for switching between five different frequencies. This frequency-switching characteristic is central to the system design, ensuring that each layer

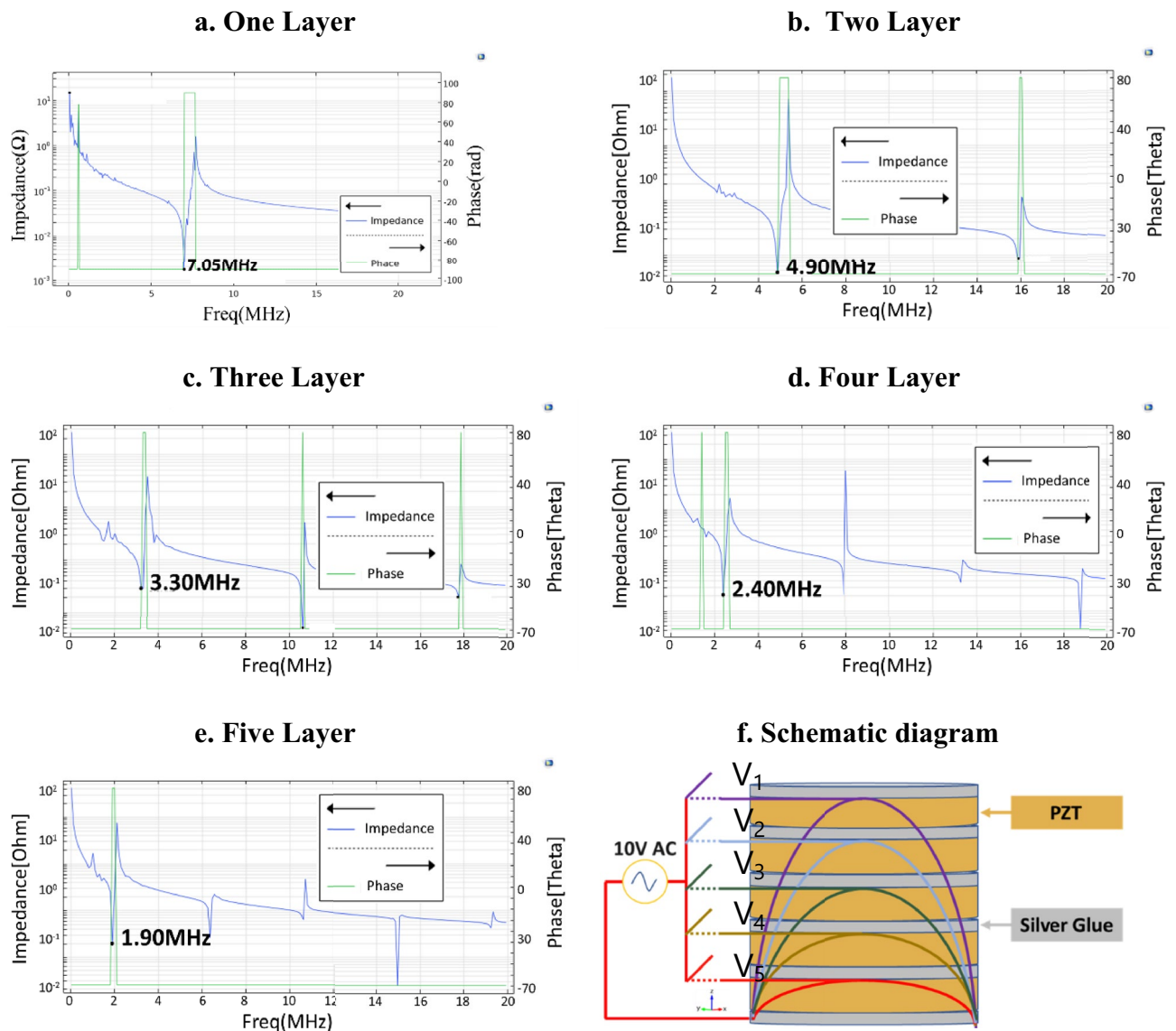


**Fig. 4.** Impedance plots of each layer of the probe. (a) First layer at 7.05 MHz. (b) Second layer at 4.9 MHz. (c) Third layer at 3.3 MHz. (d) Fourth layer at 2.4 MHz. (e) Fifth layer at 1.9 MHz. (f) Schematic diagram of a probe with each layer energized to produce a different wavelength.

operates at the appropriate frequency, thereby enabling the switching of electrical paths and signal processing at different wavelengths.

Moreover, the device design incorporates thickness and damping optimization across layers to suppress inter-layer coupling. Each PZT layer is sequentially activated, rather than simultaneously, during operation. This sequential excitation strategy substantially reduces the potential for modal interference and effectively eliminates the risk of mode hopping or energy leakage across shared mechanical boundaries.

#### Acoustic simulation frequency band mesh division

The unstructured triangular mesh method is typically used to simulate two-dimensional acoustic fields. This method can obtain a high-quality mesh covering an entire geometric structure. Unstructured triangular meshes have greater numerical diffusion than structured meshes, and they cannot model materials with high anisotropy, such as PZT material, under unbiased conditions.

Unstructured meshes generally require more refinement than structured meshes to achieve the same level of accuracy. Refining the entire mesh is typically unnecessary; local refinement of boundary regions with large geometric discontinuities is typically sufficient. This can be performed with cross-scale mesh division. In this study uses acoustic field mesh configuration for adjustment. Harmonic meshing was performed, in which the maximum frequency solution equals the central frequency of the signal multiplied by  $2^n$ . Beginning from  $2^1$ , the mesh was resolved in accordance with this maximum frequency band added. The simulation mesh type was free quadrilateral. Figure 5 presents the optimal mesh division for these frequencies.



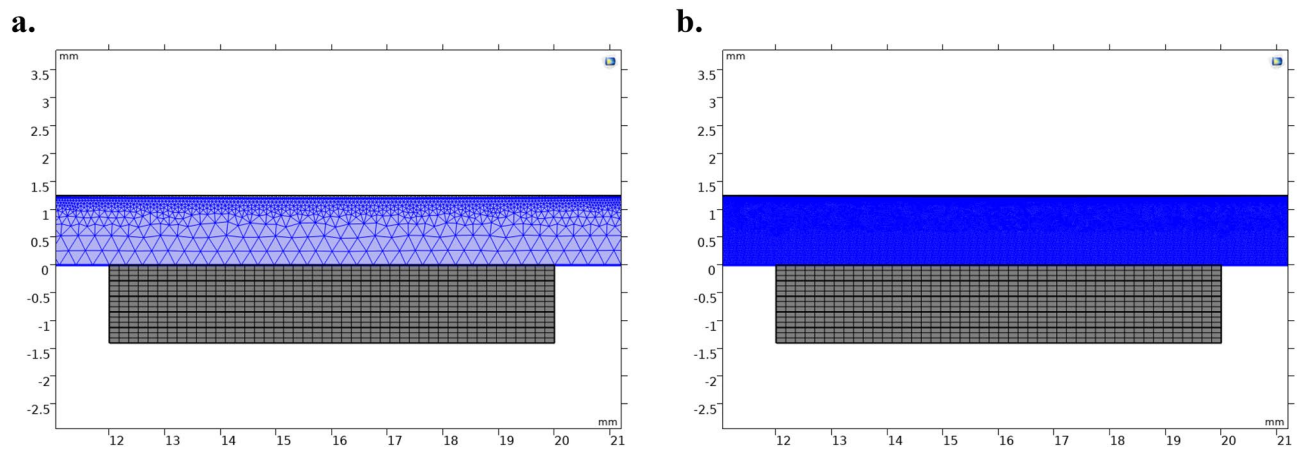


**Fig. 5.** Illustrates the schematic diagram of geometric mesh division with a height difference of 50 times in the acoustic field. Utilizing the aforementioned method for optimization. **(a)** The computation time is only 76 s, whereas employing the conventional method for calculation. **(b)** Requires 1 h and 31 min.

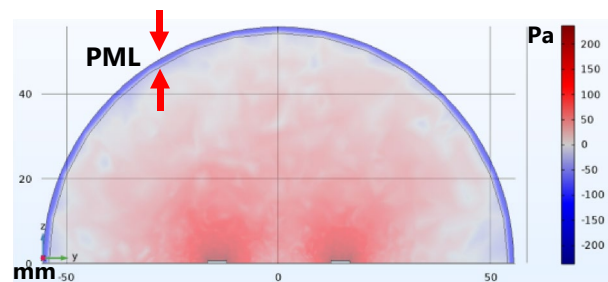


**Fig. 6.** Illustrates the perfect matching layer, PML (Blue Region). Sound pressure diagram.

### Perfectly matched layer (PML)

Incorporating a Perfectly Matched Layer (PML) to impede the transmission of acoustic waves can diminish both the computational complexity and the requisite computational duration, thereby augmenting the precision of the results. As shown in Fig. 6, the PML plays a critical role in absorbing outgoing acoustic waves and preventing artificial reflections at the domain boundaries. Rather than describing the absence of PML as causing unbounded wave propagation, it is more informative to state that the PML exerts a clear acoustic damping effect, which can be visually confirmed in COMSOL simulations. The presence of PML allows the acoustic field to remain bounded and stable, thereby validating its effectiveness.

In terms of geometry, a layered PML structure was implemented around the outer boundary. This layered form helps attenuate outgoing waves and matches the acoustic impedance profile, effectively minimizing reflections. To ensure compatibility with structured meshing in COMSOL, the shape and thickness of the PML domains were carefully constructed.

In frequency-domain models, the relationship between the operating frequency and the corresponding acoustic wavelength is the primary factor determining the effectiveness of the PML layer, rather than its absolute physical thickness. The PML thickness should be proportionally related to the wavelength to ensure proper wave absorption. Although the physical thickness influences mesh element generation, its overall impact on simulation accuracy is relatively minor.

### Echo analysis test

A needle hydrophone (designated as the receiver) is used to characterize the three-dimensional distribution of the sound field generated by the ultrasonic probe. During the measurement, the sample remains stationary while the receiver moves to different positions to capture the amplitude of the sound field emitted by the probe, thereby mapping the pressure distribution. The detailed method of the measurement process will be elaborated in subsequent chapters<sup>15,16</sup>. The hydrophone used for these measurements was the ONDA HNR-0500, a model in the HNR series that operates in the frequency range of 0.25 MHz to 10 MHz. Its physical dimensions are consistent with those depicted in the Fig. 7.

### Acoustic field simulation

According to IEC 62127-3<sup>17</sup>, the spatial position of a hydrophone must ensure that it operates within its linear acoustic response range, typically exceeding 5 MPa. In this study, the measurement distance  $x = 16.74$  mm shown

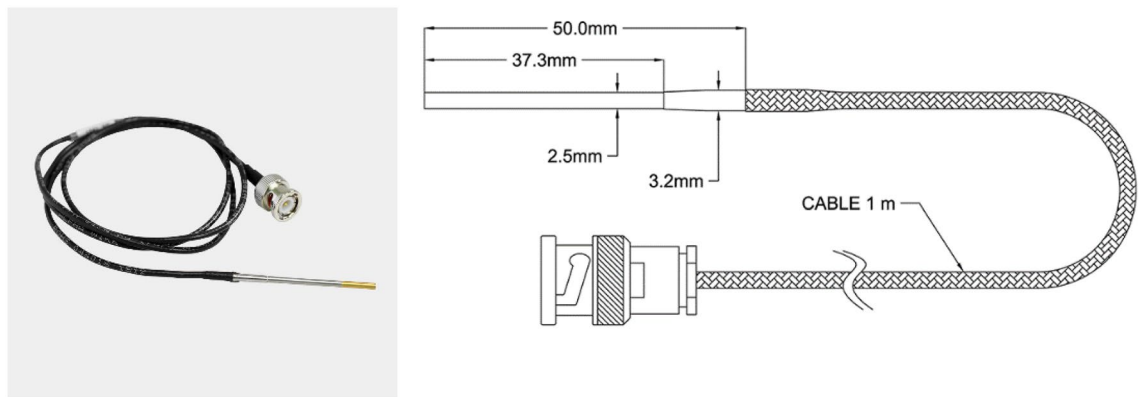


**Fig. 7.** Photograph and dimensions of the HNR-series needle hydrophone.

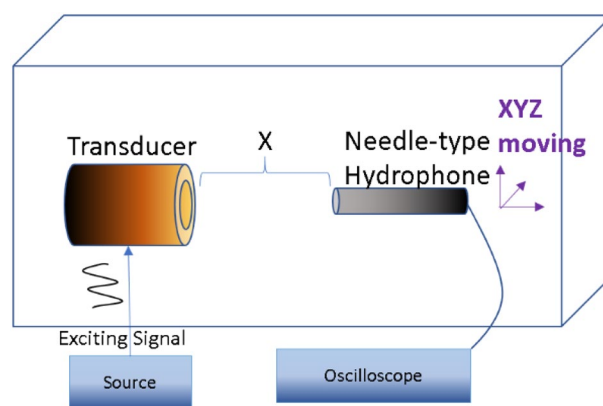


**Fig. 8.** Depicts the experimental setup for simulating extracorporeal ultrasound attenuation.

in Fig. 8 was not arbitrarily selected; it was determined based on the simulated acoustic field propagation and the transducer's frequency characteristics. Specifically, this distance corresponds to a region where the pressure field remains stable and linear for the dominant resonance frequencies of the multilayer transducer.

While not directly calculated from a single resonant wavelength, the placement takes into account the near-field and far-field transition zones of the main modes. The decision was made based on the following criteria: first, to minimize the effect of constructive interference and ensure measurement accuracy; second, to keep the pressure amplitude within the hydrophone's linear response range and avoid nonlinear distortion; and third, to ensure the angular spread of the acoustic beam is moderate and uniform, allowing for stable and representative measurements.

Therefore, the 16.74 mm distance reflects a compromise between spatial resolution, acoustic field stability, and measurement reliability, in line with both IEC standards and simulation outcomes.

The attenuation coefficients for the entire frequency band were accurately estimated using COMSOL<sup>18</sup>. However, noise also affects device performance. As a wave travels, its acoustic pressure decreases exponentially<sup>19</sup>. Fig. 9a presents a pulse wave formed by PZT. Modal oscillation was used to control the pulse signal waveform. Figure 10 illustrates simulated acoustic fields for ultrasound probe transmissions with echoes from a phantom.

In the attenuation measurement, the nonlinear propagation parameter of the receiver is less than 0.5<sup>20</sup> (Fig. 9a). If the oscilloscope can perform a frequency-domain Fourier transform, the signal received by the needle-type hydrophone without a sample in the signal's path can be expressed as Eq. (9) (10):

$$v_a(f) = R_t(f) e^{-\alpha_0 x} \quad (9)$$

$$v_b(f) = R_t(f) e^{-\alpha_0 x} e^{-(\alpha - \alpha_0)x_m} T^2 \quad (10)$$

where  $R_t$  is the transfer function of the experimental system, including the electronics and piezoelectric material,  $T$  is the transmission coefficient at the interface between the tissue and water, and  $\alpha_0$  and  $\alpha$  are the attenuation coefficients of the reference liquid and the sample, respectively. If the attenuation coefficient of the reference liquid is known, dividing these two equations and allowing the transmission coefficient  $T$  between the reference liquid and soft tissue to approach 1 can enable the calculation of the attenuation coefficient of the

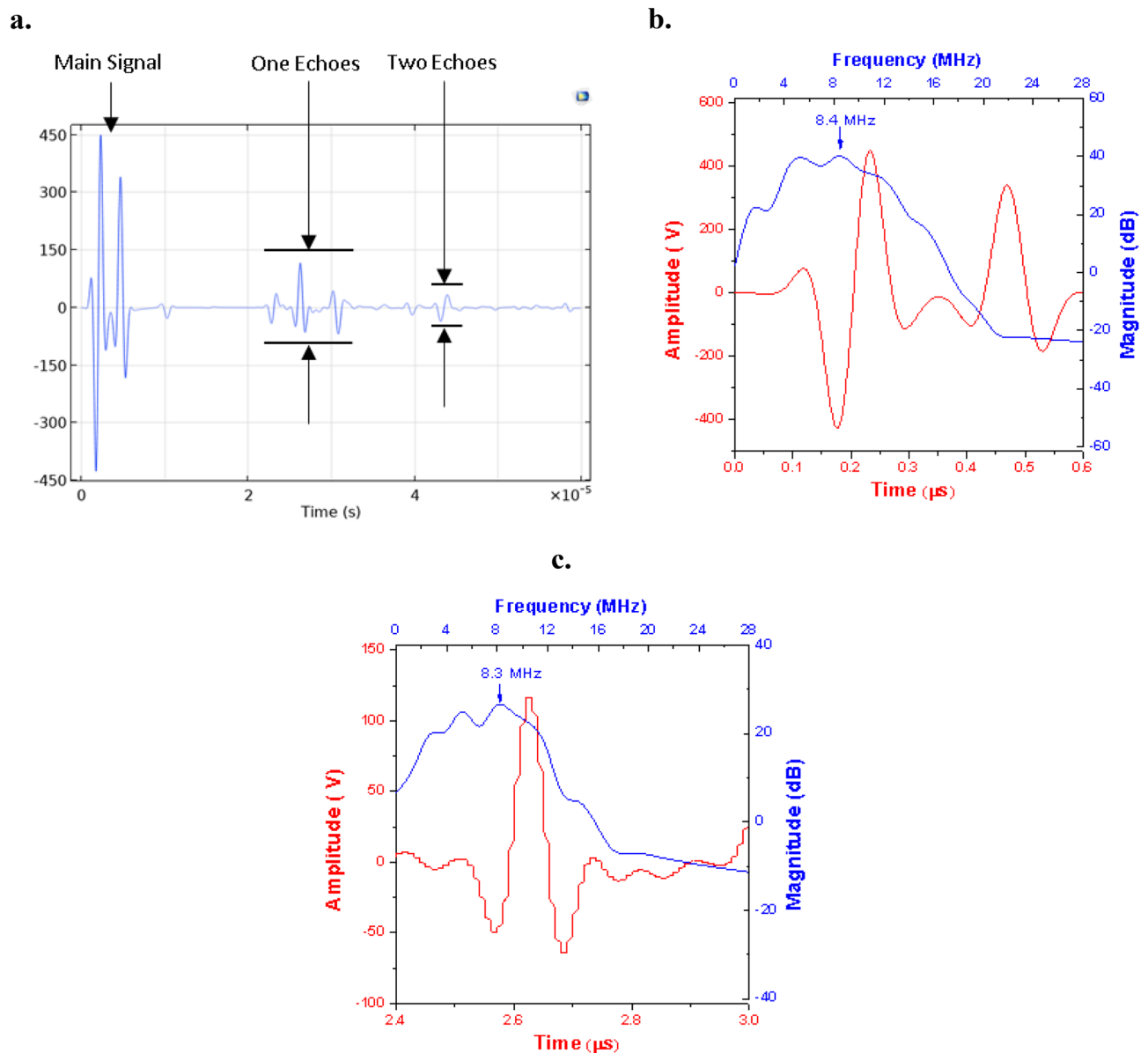


**Fig. 9.** (a) Time domain signal received by the ultrasound probe (pulse wave). (b,c) Characterization of simulation results using FFT for multi-frequency analysis.

sample as the ratio of the measured thickness of the tissue sample to that of the reference liquid. This experimental method does not require knowing the transfer function  $R_t(f)$  of the experimental system. In contrast to that of the velocity measurements, the accuracy of the thickness measurements may be too low for measuring attenuation. The sample thickness  $x_m$  can be measured manually or calculated from time difference measurements.

Figure 9b shows the primary wave emitted by the probe, with its frequency determined through FFT analysis and indicated as 8.4 MHz. This figure demonstrates the probe's capability to emit a wave at the specified frequency. Figure 9c, on the other hand, displays the echo wave received by the probe over time. The first echo, analyzed through FFT as indicated by the blue line, shows a frequency of 8.3 MHz. This result confirms that the probe successfully detected the echo of the emitted wave. The purpose of Fig. 9c is to validate the probe's capability to detect and analyze returning waves, ensuring that the frequency of the received signal is consistent with the emitted wave, demonstrating the probe's effectiveness in.

The model depicted in Fig. 10 employs a semicircular design to mimic puncturable tissue in the human body and serves as a surrogate for bone in this research. This setup is a key aspect of a significant research endeavor aimed at enhancing the precision of ultrasound prior to the insertion of an injection needle through the skin<sup>21</sup>. The apparatus utilizes A-mode ultrasound to examine both non-puncture and puncture tissues. Given that the human body is predominantly made up of water, the puncturable tissue being investigated is simulated by water.

The model comprises several essential components. The semicircular structure represents bone or other vital tissue that requires monitoring to prevent accidental injury during injection. The surrounding area consists of

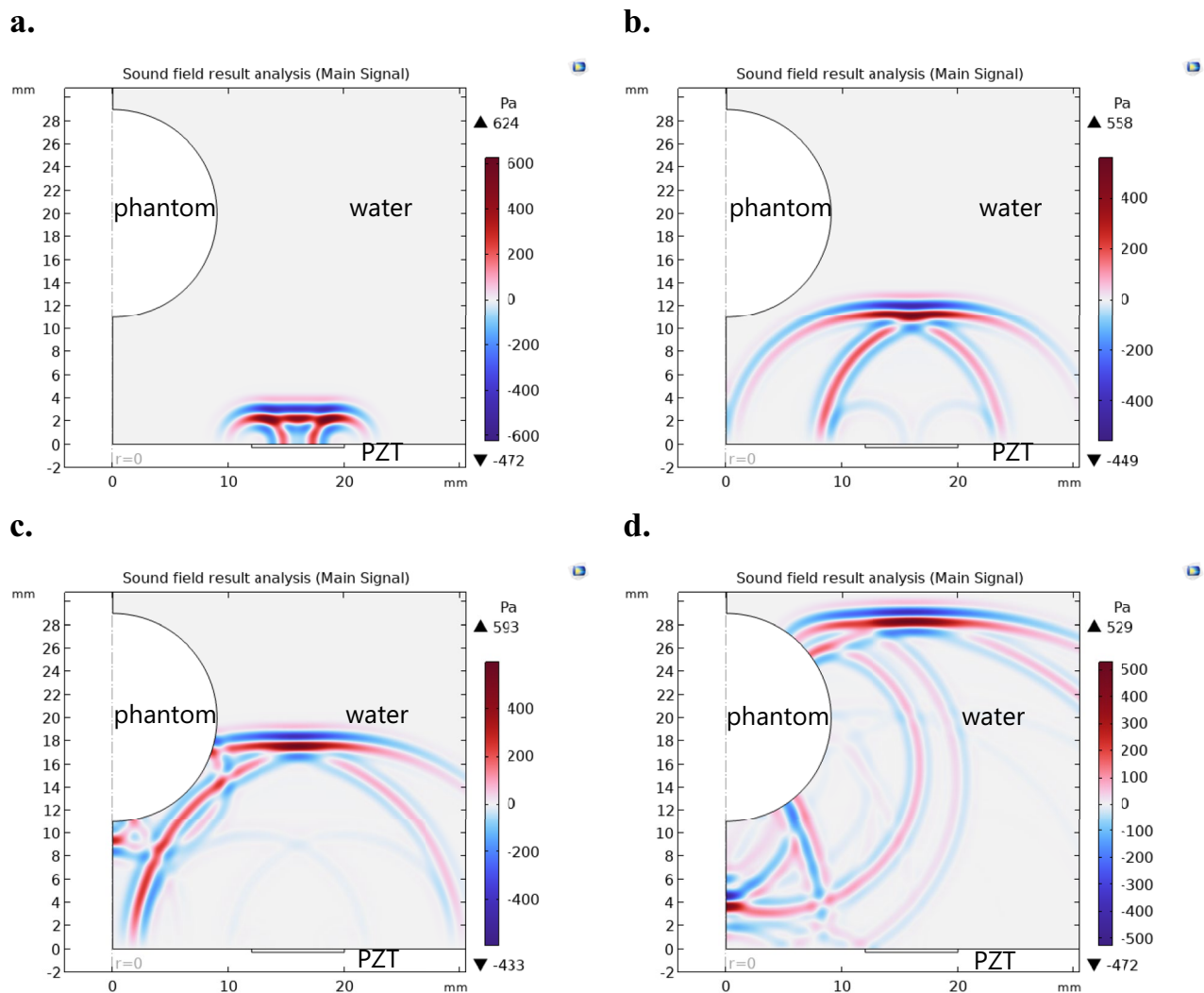


**Fig. 10.** Analysis of the probe's echo acoustic field.

water or the inner skin layer. Water is chosen due to its effective conduction of ultrasonic waves, facilitating the transmission of ultrasonic waves and resulting in clearer electrical signal outputs<sup>22</sup>. The base of the model features a PZT ultrasound probe that emits and receives ultrasound signals to generate a real-time sound field. Placing the probe in this manner ensures that the ultrasound can penetrate deep into the skin and subcutaneous tissue, producing precise electrical signals.

The selection of sensor configuration in relation to the needle is influenced by several factors. Firstly, the design and placement of the ultrasonic probe ensure precise focus on the area where the needle will penetrate, enhancing the accuracy of electrical signals. Secondly, precise positioning of subcutaneous structures is essential to avoid harm to vital structures like blood vessels, nerves, or bones during the injection process, thereby enhancing the safety of subcutaneous injections. Lastly, real-time echo signal processing can be connected to the backend database for analysis and implementation<sup>23</sup>.

In summary, the semicircular model and ultrasonic probe configuration depicted in Fig. 10 are meticulously designed to provide precise electrical signals and real-time monitoring. This aids in accurately locating subcutaneous tissue for subcutaneous injections, thus preventing potential damage and enhancing the safety and success rate of the injection<sup>24</sup>. Figures 9 and 10 from the simulation study illustrate the pulse wave output emitted by the PZT, simulating the ultrasound scanning process as it penetrates the skin and reflects from the unpunctured measurement object (bone). A-mode ultrasound effectively captured both echoes, showcasing its effectiveness in this scenario.

#### *Multilayer circuit control design*

The basic mechanical response of the PZT ceramic when an electric field was applied were measured using an impedance analyzer (Keysight's E4990A). The effective surface area of the ceramic was measured to be 765.375 mm<sup>2</sup>. To achieve rapid switching between multiple frequencies in a single channel, the core of the device

comprised single-tab convex copper plates connected to a multichannel circuit with gold layers. The device required an AC voltage supply of  $\pm 10$  V.

To further ensure the integrity of the multilayer configuration, potential parasitic interlayer capacitance was considered during the design phase. The conductive silver and copper layers between the PZT ceramic stacks were modeled based on the thickness-to-wavelength ratio to minimize capacitive coupling effects. These conductive layers were incorporated into the COMSOL simulations using impedance-matching principles, effectively capturing distributed impedance behavior across the stack. By maintaining optimized interlayer geometry and minimizing dielectric discontinuities, parasitic effects were reduced, allowing stable frequency switching between layers without signal interference. This approach ensures reliable operation in a multi-frequency environment, particularly at higher frequencies, where distributed capacitance could otherwise impact impedance consistency.

#### *Frequency and impedance verification for the sample module*

To evaluate the influence of interlayer parasitic capacitance on high-frequency performance, both simulation and experimental impedance analysis were performed across the frequency range of interest. In the COMSOL simulation phase, interlayer effects were incorporated using equivalent impedance expressions (as introduced in Eq. 2.3), capturing the interactive behavior between PZT and the conductive silver layers. These interlayer interactions were further validated using impedance measurements with the Keysight E4990A analyzer. The results showed consistent resonant and anti-resonant frequencies with minimal deviation across layers, indicating that distributed capacitance did not introduce significant impedance distortion. This consistency between simulation and experiment confirms that the probe design effectively suppresses undesired parasitic effects, maintaining reliable performance even in high-frequency switching scenarios.

The preliminary simulation results were used to create a sample model (Fig. 11). Each PZT layer had a thickness of 0.28 mm, and an additional 0.01-mm layer of silver paste was applied on both sides. The layers were rings with inner and outer radii of 12.5 and 20 mm, respectively. A 0.1-mm-thick copper conductive layer was included between each pair of PZT layers. The overall thickness of the probe was 2.4 mm (Fig. 11b). Multiple devices were created with identical parameters (Fig. 11a). The samples were examined using an impedance analysis instrument (Keysight's E4990A) with a frequency range set from 20 Hz to 20 MHz.

The first layer of sample 44 had an impedance value at 7.16 MHz (as shown in Fig. 12b). The impedance plot illustrates the impedance and phase angle of the ultrasonic probe over time, revealing the resonance and anti-resonance frequencies.

The impedance diagram consists of both a real part and an imaginary part. The real part reveals that the impedance exhibits pronounced extremes at the resonant and anti-resonant frequencies. Meanwhile, the phase angle of the imaginary part further elucidates this relationship, transitioning between  $0^\circ$  and  $90^\circ$ . The resonant frequency is more distinctly identified by analyzing the changes in the phase angle depicted in Fig. 12, specifically at the location corresponding to the assembly resistance diagram. This analysis provides valuable insights for research and facilitates the identification of resonant frequencies across various layers and sample variations, which serve as critical indicator parameters.

Simulated resonant frequencies assist in determining the resonant characteristics of the samples. This study focuses on identifying the target resonant frequency within the operational frequency range, recognizing that at the resonant frequency, multi-band coupling typically occurs. Such variability introduces uncertainty into the modal series; however, simulation proves effective in mitigating this issue. Initially, modal observations are digitized, and the resonant frequency of the first mode is highlighted. This approach enables the rapid extraction of required resonant frequencies from large datasets generated by the impedance analyzer. After rigorous verification, the resonant frequencies extracted from the impedance diagrams are summarized in Table 5, which presents the final resonant frequency for each frequency band analyzed in this study.

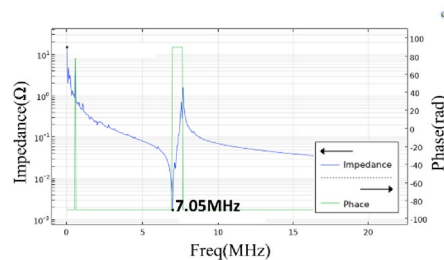
In Fig. 12a, the first layer serves as the optimal benchmark for this study. Beyond clearly highlighting the resonant frequencies, it also demonstrates exemplary variations in angular frequency, facilitating straightforward identification and observation. A comparison with the first layer in Fig. 12b reveals that the resonant frequencies in both impedance plots are remarkably similar. Notably, a frequency of 7 MHz is identified as suitable for subcutaneous injection measurements in this study. As the first layer aligns with the research objectives, it



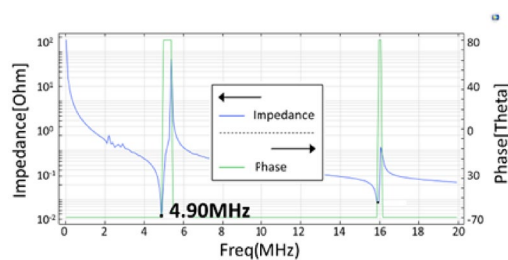
**Fig. 11.** (a) Sample size and (b) the thickness measurement using a vernier caliper.



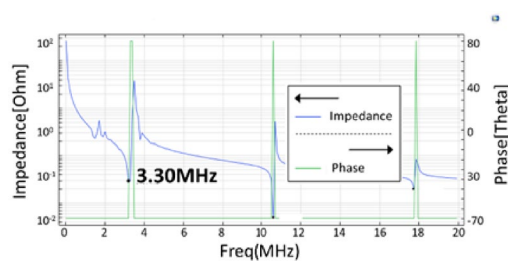
**a. Natural frequency of COMSOL  
simulation analysis  
One Layer**



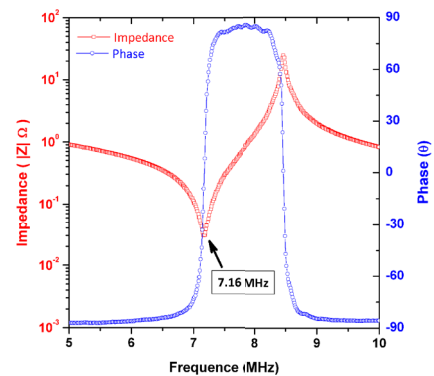
**Two Layer**



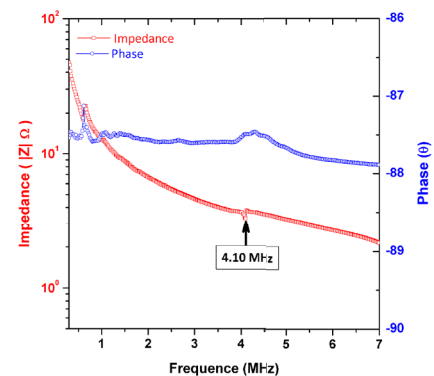
**Three Layer**



**b. Natural frequency of Impedance  
Analyzer experimental data  
Scan Range 5MHz - 10 MHz**



**Scan Range 300kHz - 7 MHz**



**Scan Range 300kHz - 4.4MHz**

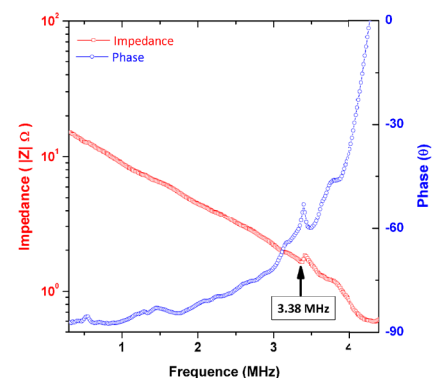


**Fig. 12.** Impedance plot of the Natural frequency comparison. 1 to 5 layers. Frequency position measured by Impedance Analyzer (Keysight's E4990A).

establishes a solid foundation for further analysis. The subsequent discussion addresses the second layer of the study. Simulation-based trend analysis predicts the center frequency range for the first layer to be approximately 7.5 MHz, with the impedance analyzer's scanning range set between 5 MHz and 10 MHz. Similarly, the second layer requires a specific measurement range, ultimately determined to be 0.3 MHz to 7 MHz. Within this range, a resonant frequency of 4 MHz is identified, yielding consistent results that align with the study's objectives. For the third layer, the prediction model centers around a resonant frequency of 3.3 MHz. To enhance observation

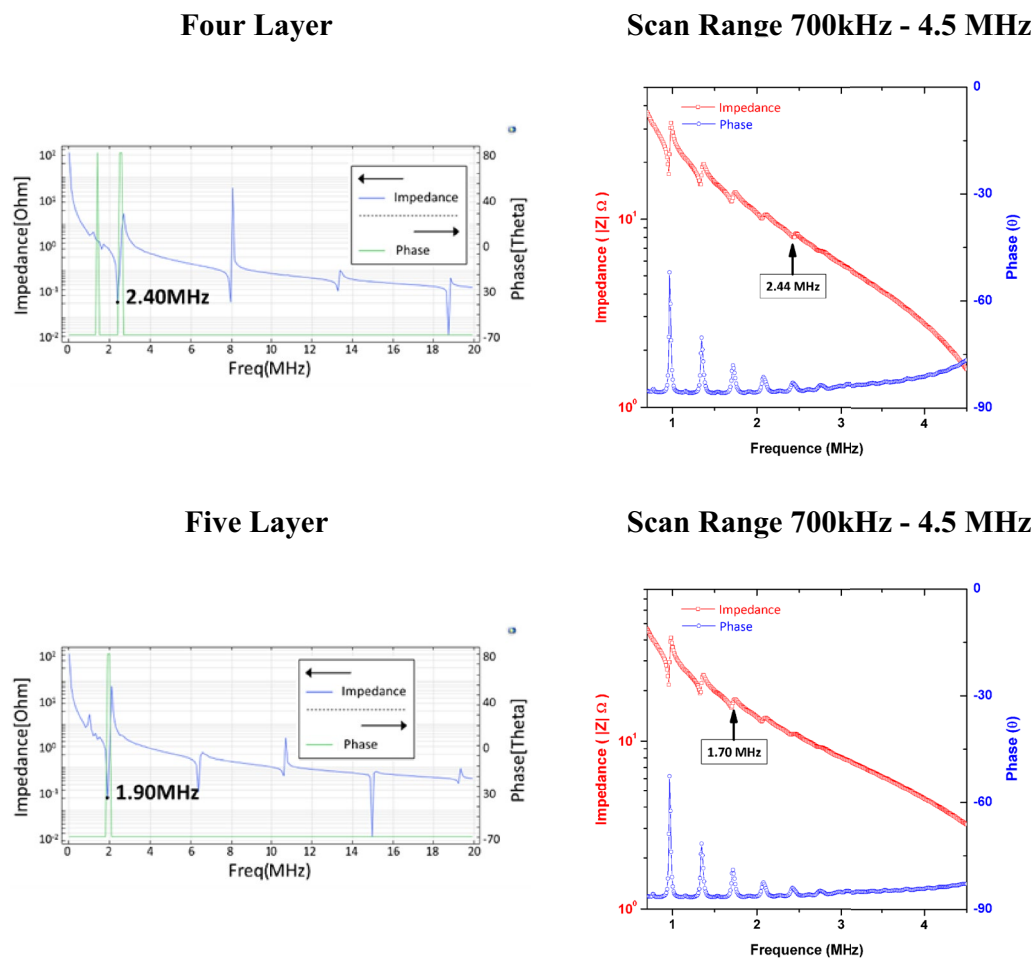


Fig. 12. (continued)

Layer	COMSOL simulation analysis	Experimental data
One	7.05 MHz	7.16 MHz
Two	4.9 MHz	4.10 MHz
Three	3.3 MHz	3.38 MHz
Four	2.4 MHz	2.44 MHz
Five	1.9 MHz	1.70 MHz

Table 5. Natural frequency comparison table.

clarity, the second-mode resonant frequency, slightly above 4.4 MHz, is excluded from the impedance plot of the third layer. Consequently, the measurement range is adjusted to 0.3 MHz to 4.4 MHz. The predicted model for the third layer closely aligns with the experimental values, demonstrating similar resonant frequencies and comparable ultrasonic measurement functions. The frequency range for the fourth layer spans 0.7 MHz to 4.5 MHz, providing favorable conditions for observation. In the model analysis of Fig. 12a, the resonant frequency is identified at 2.40 MHz, which closely corresponds to the verification data in Fig. 12b, showing a resonant frequency of 2.44 MHz, where most modes are concentrated. This consistency underscores the utility of the predicted trend in supporting the observation of results. Final calibration confirms the resonant frequency in Fig. 12b as 2.44 MHz. The fifth layer employs the same frequency range as the fourth, with a predicted resonant frequency close to 1.70 MHz. This prediction meets the research requirements and fulfills the necessary conditions, yielding results that are both consistent and insightful. Finally, the resonant frequencies for all five layers are summarized in Table 5, providing a comprehensive reference for the study's findings.

To ensure the independence of each target mode, finite element simulations incorporated both modal and harmonic response analysis. The vibration profile of each PZT layer was carefully evaluated to verify that the energy was well-confined within individual modes. This verification ensures that the displacement distribution of each mode remains distinct, minimizing undesired interactions across layers.

### Thermal evaluation consideration

Although this study primarily focuses on the mechanical resonance characteristics and impedance behavior of the multilayer PZT stack under MHz-frequency excitation, thermal effects—particularly those caused by dielectric losses—have not been explicitly modeled or measured in the current phase. The experimental setup used low-voltage, short-pulse excitations ( $\pm 10$  V), which limited continuous energy accumulation and thus minimized immediate thermal concerns.

However, as part of our future research direction, we plan to incorporate both finite element-based thermal simulations and non-contact infrared thermography to investigate the surface temperature distribution and potential thermal buildup under prolonged excitation. This will enable us to comprehensively assess the thermal reliability of the probe design and its long-term operating stability in clinical environments.

## Conclusion

PZT ceramic layers were successfully integrated to develop a multilayer, frequency-switching ultrasound probe. Parameterized modeling was conducted using COMSOL Multiphysics to design the probe, establish coupling between physical fields, and optimize probe parameters. Stable switching between probe signals and circuits was achieved by ensuring an accurate voltage supply, a critical factor for stable circuit operation. The device was determined to operate with an AC voltage of  $\pm 10$  V. An optimized mesh configuration was developed to obtain peak displacement data and facilitate rapid adjustments to the thickness and other structural dimensions of the simulated samples.

The designed circuit allowed for flexible selection and adjustment of frequency bands according to experimental requirements, resulting in a probe with high efficiency and penetration at varying frequencies. The multilayer ceramic structure and circuit design were further optimized to achieve precise control of frequency and impedance, ensuring excellent performance across diverse application scenarios.

Experimental validation demonstrated that the probe meets the requirements for ultrasonic detection and imaging applications, as confirmed through comparisons with COMSOL simulation results. Impedance measurements revealed the influence of microstructural characteristics on stress fields. Furthermore, the experimental and simulated natural frequencies of individual layers showed favorable agreement.

In summary, the designed multilayer ultrasound probe represents a reliable and efficient solution for various ultrasonic applications, combining robust performance with versatile functionality.

## Data availability

For any questions or requests for data regarding this study, please contact the corresponding author, Yu-Lin Song (Email: d87222007@ntu.edu.tw). This statement has been provided both in the submission system and in the manuscript file.

Received: 4 December 2024; Accepted: 17 June 2025

Published online: 01 July 2025

## References

1. Serup, J., Bove, T., Zawada, T., Jessen, A. & Poli, M. High-frequency (20 MHz) high-intensity focused ultrasound: new treatment of actinic keratosis, basal cell carcinoma, and Kaposi sarcoma. An open-label exploratory study. *Skin. Res. Technol.* **26** (6), 824831 (2020).
2. Bezugly, A. & Rembielak, A. The use of high frequency skin ultrasound in nonmelanoma skin cancer. *J. Contemp. Brachytherapy.* **13** (4), 483491 (2021).
3. Li, H. et al. Highfrequency ultrasound of the skin in systemic sclerosis: an exploratory study to examine correlation with disease activity and to define the minimally detectable difference. *Arthritis Res. Ther.* **20**, 181. <https://doi.org/10.1186/s1307501816869> (2018).
4. Liu, Y. et al. Gaussian processes with normalmodebased kernels for matched field processing. *Appl. Acoust.* **220**, 109954 (2024).
5. Rong, S. H. U. Design and performance research of micro linear piezoelectric motor base on thin plate. *J. nanchanghangkonguniversity(Natural Sci. edition)*. **35** (3), 8691. <https://doi.org/10.3969/j.issn.20968566.2021.03.014> (2021).
6. Shung, K. K. *Diagnostic Ultrasound Imaging and Blood Flow Measurements* (1st ed.) <https://doi.org/10.1201/9780849338922> (2005).
7. Ciba, S., Frey, A. & Kuehne I. *Analysis of Geometrical Aspects of a Kelvin Probe*. (2016).
8. Martins, M. S. et al. Wideband and wide beam polyvinylidene difluoride (PVDF) acoustic transducer for broadband underwater communications. *Sensors* **19** (18), 3991 (2019).
9. Zawada, T. & Bove, T. Analytical modeling of harmonically driven focused acoustic sources with experimental verification. *Appl. Acoust.* **221**, 109989 (2024).
10. Kaltenbacher, M. *Numerical Simulation of Mechatronic Sensors and Actuators* vol. 2 (Springer, 2007).
11. Yanhong, L. I. U., Binghua, W. A. N. G. & Guanghui, Q. I. N. G. Free vibration analysis of piezoelectric laminated plates with delamination. *Eng. Mech.* **29** (7), 347352 (2012).
12. The study of segmental body composition using fuzzy theory and bioimpedance. Foster, K. R. & Lukaski, H. C. (1996). Whole-body impedance—what does it measure? *Am. J. Clin. Nutr.* **64**(3), 388S–396S. (2000).
13. Yao, Z., Hu, H., Gao, L., Zhang, S. Analysis of influence of mesostructure characteristics on internal stress field of piezoelectric stack. *Piezoelectrics & Acousto-optics*, **45**(4). (2023).
14. Sharifi, M. & Karafi, M. Development of a contact layer in the finite element model of ultrasonic transducers to evaluate losses in contact surfaces. *Appl. Acoust.* **211**, 109455 (2023).
15. GarzaAgudelo, D. M. et al. Metasurfaces for sound absorption over a broad range of wave incidence angles. *Appl. Acoust.* **220**, 109965 (2024).
16. Harris, G. R. A model of the effects of hydrophone and amplifier frequency response on ultrasound exposure measurements. *IEEE Trans. Ultrason. Ferroelectr. Freq. Control.* **38** (5), 413–417 (1991).
17. IEC 62127. Measurement and characterization of medical ultrasonic fields up to 40 mhz. *Int. Electrotechnical Comm.*, (2007).
18. Dubus, B., Croëne, C. & Mosbah, P. Modeling of power ultrasonic transducers. In *Power Ultrasonics*, 147159 (Woodhead Publishing, 2023).
19. Sherman, C. H. & Butler, J. L. *Transducers and Arrays for Underwater Sound* (Springer, 2007).

20. Lasky, M. Review of undersea acoustics to 1950. *J. Acoust. Soc. Am.* **61**, 283–297 (1976).
21. Givoli, D. & Neta, B. Highorder nonreflecting boundary scheme for timedependent waves. *J. Comput. Phys.* **186** (1), 2446 (2003).
22. Shariati, B. K., Ansari, B. & Khatami, M. A. Multimodal optical clearing to minimize light Attenuation in biological tissues. *Sci. Rep.* **13**, 21509. <https://doi.org/10.1038/s4159802348876x> (2023).
23. Marina, M. E. et al. Highfrequency sonography in the evaluation of nail psoriasis. *Med. Ultrasonography.* **18** (3), 312317 (2016).
24. Blackstock, D. T. *Fundamentals of Physical Acoustics* (Wiley, 2000).

## Acknowledgements

This study received support from contracts with Asia University Hospital, National Taiwan University, SHL Medical and COMSOL PITOTECH CO.

## Author contributions

Yu-Lin Song, Shih Hsun Tu and Alexander Stiegler: Conceptualization, Yu-Lin Song: Methodology, Yu-Lin Song and Tzu-Zin Lin: Software, Yu-Lin Song and Alexander Stiegler: Investigation, Yu-Lin Song, Shih Hsun Tu and Alexander Stiegler: Writing- Reviewing and Editing, Yu-Lin Song: Validation, Yu-Lin Song: Supervision. Tzu-Zin Lin: Data curation, Tzu-Zin Lin: Writing- Original draft preparation, Software, Investigation.

## Declarations

## Competing interests

The authors declare no competing interests.

## Additional information

**Correspondence** and requests for materials should be addressed to Y.-L.S.

**Reprints and permissions information** is available at [www.nature.com/reprints](http://www.nature.com/reprints).

**Publisher's note** Springer Nature remains neutral with regard to jurisdictional claims in published maps and institutional affiliations.

**Open Access** This article is licensed under a Creative Commons Attribution-NonCommercial-NoDerivatives 4.0 International License, which permits any non-commercial use, sharing, distribution and reproduction in any medium or format, as long as you give appropriate credit to the original author(s) and the source, provide a link to the Creative Commons licence, and indicate if you modified the licensed material. You do not have permission under this licence to share adapted material derived from this article or parts of it. The images or other third party material in this article are included in the article's Creative Commons licence, unless indicated otherwise in a credit line to the material. If material is not included in the article's Creative Commons licence and your intended use is not permitted by statutory regulation or exceeds the permitted use, you will need to obtain permission directly from the copyright holder. To view a copy of this licence, visit <http://creativecommons.org/licenses/by-nc-nd/4.0/>.

© The Author(s) 2025